Discover Nano

Research

Revolutionizing radiotherapy: gold nanoparticles with polyphenol coating as novel enhancers in breast cancer cells—an in vitro study

Simona Tarantino[1] · Annalisa Bianco[1] · Mariafrancesca Cascione[1,2] · Alessandra Carlà[3] · Lia Fiamà[3] · Riccardo Di Corato[2,4] · Livia Giotta[5] · Paolo Pellegrino[2] · Anna Paola Caricato[1] · Rosaria Rinaldi[1,2] · Valeria De Matteis[1,2]

Received: 2 September 2024 / Accepted: 8 January 2025
Published online: 15 January 2025

Abstract
Breast cancer is the most common cancer among women, with over 1 million new cases and around 400,000 deaths annually worldwide. This makes it a significant and costly global health challenge. Standard treatments like chemotherapy and radiotherapy, often used after mastectomy, show varying effectiveness based on the cancer subtype. Combining these treatments can improve outcomes, though radiotherapy faces limitations such as radiation resistance and low selectivity for malignant cells. Nanotechnologies, especially metallic nanoparticles (NPs), hold promise for enhancing radiotherapy. Gold nanoparticles (AuNPs) are particularly notable due to their high atomic number, which enhances radiation damage through the photoelectric effect. Studies shown that AuNPs can act as effective radiosensitizers, improving tumor damage during radiotherapy increasing the local radiation dose delivered. Traditional AuNPs synthesis methods involve harmful chemicals and extreme conditions, posing health risks. Green synthesis methods using plant extracts offer a safer and more environmentally friendly alternative. This study investigates the synthesis of AuNPs using *Laurus nobilis* leaf extract and their potential as radiosensitizers in breast carcinoma cell lines (MCF-7). These cells were exposed to varying doses of X-ray irradiation, and the study assessed cell viability, morphological changes and DNA damage. The results showed that green-synthesized AuNPs significantly enhanced the therapeutic effects of radiotherapy at lower radiation doses, indicating their potential as a valuable addition to breast cancer treatment.

1 Introduction

Breast cancer is the most prevalent cancer among women, with over 1 million new cases and approximately 400.000 deaths reported globally each year, according to the World Health Organization [1]. Consequently, this illness is one of the most significant and expensive health challenges worldwide. Chemotherapy and radiotherapy (RT) can be employed either before or after mastectomy for cancer treatment [2]. Specifically, neoadjuvant chemotherapy is often used in patients with locally advanced breast cancer to reduce tumor size before surgery, allowing for more conservative surgical options and improving operability [3]. Similarly, neoadjuvant radiotherapy, although less commonly used, may be

✉ Valeria De Matteis, valeria.dematteis@unisalento.it | [1]Department of Mathematics and Physics "Ennio De Giorgi", University of Salento, Via Arnesano, 73100 Lecce, LE, Italy. [2]Institute for Microelectronics and Microsystems (IMM), CNR, Via Monteroni, 73100 Lecce, Italy. [3]Oncological Center, "Vito Fazzi" Hospital of Lecce, Piazza Filippo Muratore 1, 73100 Lecce, Italy. [4]Center for Biomolecular Nanotechnologies, Istituto Italiano Di Tecnologia (IIT), 73010 Arnesano, Italy. [5]Department of Biological and Environmental Sciences and Technologies (DiSTeBA), University of Salento, Via per Monteroni, 73100 Lecce, Italy.

considered in specific cases to enhance local control, particularly in cases where the tumor is fixed to the chest wall or there are concerns about achieving negative surgical margins [4].

The effectiveness of X-ray therapy varies depending on the breast cancer subtype. Combining these treatments can significantly enhance therapeutic outcomes [5]. Therefore, radiotherapy for breast cancer can reduce its efficiency and affect normal tissues for several reasons. Among these the radiation resistance induces the loss of susceptibility to damage from the treatment and the low selectivity to malignant cells.

In the pursuit of new strategies to enhance the effectiveness of radiotherapy at tumor sites, nanotechnologies offer promising potential due to their unique properties. [6–8].

Nanomaterials, especially metallic nanoparticles (NPs), are emerging as pivotal tools in revolutionizing the treatment of severe diseases, including cancer [9]. In particular, gold nanoparticles (AuNPs) have garnered and continue to receive considerable attention due to their physicochemical properties. Au has a high atomic number (Z = 79), that significantly amplify targeted radiation damage in both in vitro and in vivo settings. This enhancement is believed to occur through the photoelectric effect, which results in the emission of short-range Auger electrons and characteristic X-rays. These properties make AuNPs particularly suitable for radiotherapy (RT). [10, 11]. Indeed, AuNPs acting as effective radiosensitizers against cancer cells when exposed to RT significantly enhancing tumor damage in the localized site [12].

Additionally, the action of cancer-incubated and irradiated metallic NPs triggers biological mechanisms such as the suppression of thioredoxin reductase activity [13]. This is significant because numerous tumor cells express elevated levels of Thioredoxin (Trx) and thioredoxin reductase (TrxR), which may contribute to drug resistance during tumorigenesis. Therefore, inhibiting the Trx system could play a role in enhancing cancer therapy and improving the efficacy of chemotherapeutic agents [14], and equally important the radio sensitizing activity of metal NPs [15].

In literature, different kinds of AuNPs were used in combination with radiotherapy. Different works demonstrated the effectiveness of this kind of nanomaterial.

Wu et al. [16] conjugated $(RGD)_4$ peptides on polyethylene glycolylated (PEGylated) 15 nm AuNPs (P-AuNPs) (RGD/P-AuNPs), and tested them on three breast cancer cell lines such as MDA-MB-231, Hs578T and SK-BR-3. After irradiating at 130 kV with doses up to 4 Gy, they found that RGD/P-AuNPs enhanced radiation effects by inhibiting the invasive activity of breast cancer cells.

Teraoka et al. [17] conducted an in vitro study on the impact of AuNPs in RT, using the HSC-3 cell line derived from human head and neck carcinoma. Cancer cells were exposed to 5 nm AuNPs at four concentrations of 0.1 nM, 0.4 nM, 1.0 nM and 10 nM. The cell count was reduced to 50%, with the most significant effects at 4 Gy and 8 Gy radiation levels.

Rahman et al. [18] performed experiments on bovine aortic endothelial cells to simulate endothelial tissue and assessed cell survival as a measure of dose enhancement. They observed dose enhancement factors, based on 90% cell survival, ranging from 4 to 25 at concentrations between 0.25 mM and 1 mM when cells were exposed to an 80 kVp x-ray beam.

Also in vivo, the effectiveness of AuNPs were demonstrated. Aditi et al. [19] investigated the radiosensitization effects of hollow AuNPs (50 nm diameter and 35 nm shell thickness) on 4 groups of mice bearing triple-negative breast cancer (TNBC) MDA-MB-231 xenografts. They injected 2.8 mg of AuNPs per gram of tumor tissue and irradiated with a single dose of X-rays (10 Gy, 225 kVp), resulting in a significant tumor growth delay compared to the control group.

Sato et al. [20] observed that the in vivo combination of 1.0 nM, cetuximab, and 4 Gy RT in a xenograft model of head and neck squamous cell carcinoma (HSC-3 cells) implanted into nude mice (BALB/cAJcl-nu/nu) led to a reduction in tumor volume compared to the control group.

However, the conventional methods for synthesizing AuNPs often involve physical or chemical processes that can negatively impact human health. These methods typically use harmful chemical reagents, solvents, and require specific reaction conditions like high temperatures or extreme pH values [21–23].

A potentially beneficial breakthrough for human health is represented by biological AuNPs synthesis methods, called "green synthesis", that employ extracts derived from plants [24].

In particular, we used *Laurus Nobilis* leaves extract since the leaves have been found to contain high levels polyphenols that contribute to their strong antioxidant activities, which surpass those of many other Mediterranean plants commonly used for similar purposes [25–29]. These polyphenols form a stable shell around the AuNPs, enhancing their therapeutic potential. Moreover, the advantages of using plant-derived extracts encompass low cost, eco-friendly agents, short reaction time, biocompatibility and large-scale production [30–32].

Green-synthesized AuNPs are currently being explored for various medical treatments, such as photothermal therapy (PTT) [33–35]. However, their potential in the context of radiotherapy (RT) remains largely unexplored. For this reason, in this study we synthesized green multi-shaped AuNPs derived from *Laurus nobilis* leaves extract to investigate their

radio sensitizing effect on breast carcinoma cell lines (MCF-7) subjected to RT. MCF-7 is the most used xenograft model of breast cancer by far. It is estrogen receptor (ER) positive, progesterone receptor positive and HER2 negative, which are features commonly seen in luminal subtype breast cancers [36, 37].

The AuNPs obtained were both spherical and triangular as well as stable in water solution. Then, starting from chemical and morphological integrity after X-rays irradiation, ensuring that they did not exhibit any kind of alterations [38], we proceeded to assess the synergistic effects of green AuNPs (0.23–30 µg/mL) and X-rays irradiation at different doses (from 2.67 to 10 Gy) on breast cancer cells in vitro. By testing cell viability, cell morphological alteration and DNA damage, we obtained promising results in the use of this type of NPs for radiotherapy increasing the therapeutic dose using a lower dose of radiation. In particular, the synergistic effect of combining spherical and triangular green AuNPs can significantly enhance the efficacy of cancer treatments, particularly when used in conjunction with radiotherapy. This combination optimizes both cellular uptake and the therapeutic impact of radiation, leveraging the distinct advantages of each nanoparticle shape. When spherical and triangular AuNPs are used together, their different internalization pathways can result in greater overall NP accumulation within tumor cells.

2 Materials and methods

2.1 Synthesis of AuNPs by green chemistry

The synthetic route of green AuNPs was adopted from the protocol described in [37]. Briefly, leaves of *Laurus nobilis* were washed with MilliQ water to remove contaminants and dried at room temperature for 24 h. Then, 25 g of leaves were finely cut and added in a beaker containing 250 mL of MilliQ water to prepare a 10% laurel solution. The mix was boiled at 100 °C for 20 min and successively it was cooled down to room temperature for 24 h. The extract was filtered with Whatman No. 1 filter paper before use for NPs synthesis.

$HAuCl_4$ aqueous solution was prepared at a concentration of 1 mM to which it was added 5 mL of *Laurus nobilis* extract previously purified to obtain a ratio of 1:4. The solution was placed on a stirrer (300 rpm) for 1 h (temperature 60 °C). In this time range, the solution color changed into a wine-red color. Subsequently, the mix was centrifuged at 3300 rpm for 85 min at 13 °C, then washed three times with MilliQ water through three cycles of centrifugation, and finally Amicon Ultra Centrifugal 3 k Filters ($HAuCl_{4,}$ Sigma-Aldrich, Dorset, UK) were used for 20 min at 13,400 rpm to collect AuNPs.

2.2 Transmission electron microscopy (TEM), X-ray diffraction (XRD) and UV–vis spectroscopy

TEM analysis of green AuNPs was performed with a JEOL JEM-1011 transmission electron microscope at 100 kV operating voltage, equipped with a 7.1 megapixel CCD camera (Orius SC1000, Gatan, Pleasanton, CA). TEM image analysis was achieved with Gatan Digital Micrograph™ (DM) software. For sample preparation, a few drops of a concentrated NPs suspension were dropped on a Formvar-coated copper grid and analyzed after complete drying. X-ray diffraction analysis was performed in Bragg–Brentano reflection geometry using filtered Cu-Ka radiation. The X-ray diffraction data were collected at a scanning rate of 0.02 degrees per second in 2θ ranging from 20 to 80° by step scanning. The ultraviolet–visible (UV–vis) spectroscopy analysis in the spectral range of 300–800 nm was performed at room temperature using a Varian Cary 5 spectrophotometer (ZEN3600; Malvern Instruments Ltd.) equipped with a quartz cuvette having 10 mm path.

2.3 Inductively coupled plasma—optical emission spectroscopy

2.3.1 The concentrations of the green AuNPs in terms of Au concentration were calculated by elemental analyses using an ICP-OES Perkin Elmer AVIO 500

For Au concentration, 200 µL of the AuNPs solution was digested overnight by adding 2 mL of aqua regia ($HCL:HNO_3$, 3:1), followed by dilution with MilliQ water (1:5).

2.3.2 First, 1×10^5 of MCF-7 were seeded in 1 mL of the medium in a 6-well plate

After 24 h at 37 °C, the medium was replaced with a fresh medium containing the AuNPs@polyphenols at a concentration of used for MTT assay. After 48 h of incubation at 37 °C, the culture medium was removed, and the cells were washed with PBS to eliminate non-internalized NPs. The cells were detached with trypsin and counted using an automatic cell counting chamber. Then, 360,000 cells were suspended in 200 µL of MilliQ water and digested by *aqua regia*. After dilution with MilliQ water, the solution was analyzed to evaluate the Au content. Elemental analysis was carried out using an ICP-OES Perkin Elmer AVIO 500.

2.4 Fourier transform infrared (FTIR) characterization

A Fourier Transform Infrared (FTIR) spectrophotometer (Spectrum One model, Perkin Elmer, Waltham, MA, USA) was used for spectra acquisitions in the mid-infrared. This spectrometer is provided with a universal accessory for attenuated total reflectance (ATR). A three-bounce diamond microprism (4 mm diameter) is the internal reflection element (IRE). Generally, a drop of about 2 µL of green AuNPs was deposited on the ATR crystal and, once the solvent was evaporated, the acquisition of ATR-FTIR spectra was proceeded at 4 cm^{-1} resolution [39]. For each spectrum, a total of 16 interferograms were then recorded and averaged. The background spectrum was registered with the bare diamond microprism.

2.5 DLS and ζ-potential

A Zetasizer Nano-ZS equipped of a HeNe laser (4.0 mW) and working at a 633 nm detector (ZEN3600, Malvern Instruments Ltd., Malvern, UK) was used for the DLS and ζ-Potential acquisitions. Measurements were performed in aqueous solutions (25 °C, pH 7). 500 green AuNPs were fitted with a normal Gaussian function to obtain the statistical size distribution of the NPs.

2.6 Irradiation set-up

The X-rays' irradiation was performed with a Elekta Precise linear accelerator operating with 6 MV photon beams. The irradiated samples were placed in a reproducible fixed set-up, consisting of an upper plate of water-equivalent material and a lower base composed of two plates with thicknesses of 1 and 0.5 cm, respectively, required to achieve the buildup for the beam energies utilized (Figure 1).

The accelerator was calibrated at 105 cm from the source to the chamber, with a depth of 5 cm and a field size of 10 x 10 cm. In this setup, 100 Monitor Units (MU) equate to a dose of 100 cGy with MU being the unit used to measure the radiation dose delivered by the accelerator. The MU values were calculated for each configuration, considering the distance from the source and the size of the radiation field.

2.7 X-ray irradiation

Once the MCF-7 cells were cultured in either 96-multiwall (96-MW) plates and/or petri dishes, depending on the treatment under investigation, they were incubated with green AuNPs at various concentrations (from 0.23 to 30 µg/mL) and subsequently irradiated at the Department of Radiotherapy of the 'Vito Fazzi' Hospital (Lecce, Italy). The administered doses were 2.67, 4, 6, 8 and 10 Gy, each of which was delivered to a single MW and/or petri dishes to evaluate its effect in the individual treatment.

For the treatment plans, a microwave (MW) device was placed between the water-equivalent bases, and a CT scan was performed. Four beams, each measuring 5 cm x 5 cm, were used and oriented at angles of 0°, 90°, 180°, and 270°. The plan was then calculated for the different prescribed doses using the Oncentra Treatment Planning System.

The treatment plans comprised direct beam configuration with gantry and collimator positioned at 0°, featuring a field size of 20 x 20 m. The MU corresponding to each prescription were delineated in Table 1. Furthermore, a three-dimensional rendering of the housing set-up, incorporating the input of the irradiation beam, was presented in Figure 2.

Fig. 1 Set-up irradiation with Elekta Precise linear accelerator on petri dishes (white arrow)

Table 1 MU values administered by the accelerator according to the specified treatment requirements

Prescription (Gy)	MU
2.67	260
4	389
6	583
8	779
10	972

2.8 MCF-7 cell culture

Human breast cancer cells (MCF-7, ATCC HTB-22^{TM}) were cultured in Dulbecco's Modified Eagle Medium (DMEM) (Sigma Aldrich, Dorset, UK) supplemented with 2 mM L-glutamine, 100U/ml of penicillin–streptomycin (Sigma-Aldrich, Dorset, UK) and 10% (v/v) fetal bovine serum (FBS, Sigma Aldrich, Dorset, UK). The cells were incubated in a humidified controlled atmosphere at 37°C in 5% CO_2.

2.9 Cell viability assay (MTT)

The cell viability assay allowed to evaluate the cells metabolic activity upon RT both with and without green AuNPs. Cell Counting Kit—8 (cod. 96992 Sigma-Aldrich, Dorset, UK) that utilizes the highly water-soluble tetrazolium salt WST-8 [2-(2-methoxy-4-nitrophenyl)−3-(4-nitrophenyl)−5-(2,4-disulfophenyl)−2H-tetrazolium, monosodium salt] was used and left to incubate in wells for 1 h. 2.5 x 10^3 cells per well were seeded onto 96 multiwell culture plates with various green AuNPs concentrations (ranging from 0.23 µg/mL to 30 µg/mL), always with two columns available for control, namely MCF-7 without AuNPs. After 48 h from NPs-treatment, each MW was irradiated with a specific

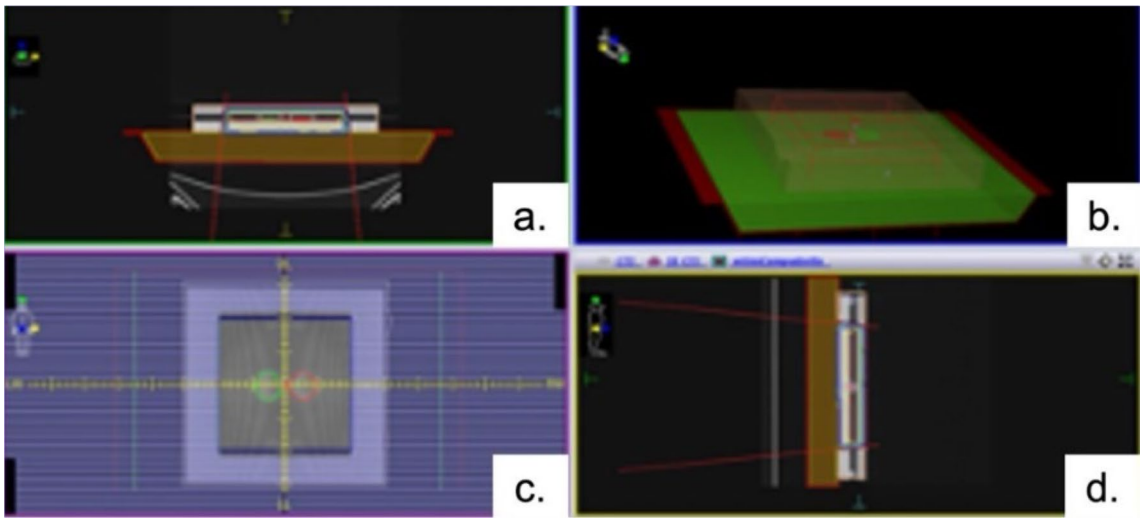

Fig. 2 **A** Axial and **D** sagittal images of the dose distribution in the sample positioned between the two water-equivalent bases; **B** 3D image of the housing set-up; **C** view from the gantry (Beam Eye View – BEV)

radiation dose among those cited before and left 24 h to incubate. Untreated and non-irradiated controls consisted of 96 multiwell with MCF-7 alone incubated for 72 h. A WST-8 assay was performed following the procedure described in a datasheet. The absorbance values were read at 450 nm with BioTek Gen5™ Microplate Reader (Agilent Technologies, Inc.). The data were expressed as a mean ± SD.

2.9.1 Confocal analysis

Laser scanning confocal microscopy was used on a Zeiss LSM700 (Zeiss) confocal microscope equipped with an Axio Observer Z1(Zeiss) inverted microscope using ×100, 1.46 numerical aperture oil immersion lens for imaging. Confocal data were processed using ZEN2010 software (Zeiss). Prior to confocal analysis, 6.2 x 10^4 MCF-7 cells/petri were seeded in 50 x 7 mm glass petri dishes (WillCo Wells B.V., 1054SE Amsterdam). After 24 h the cells were incubated with green AuNPs (0,46 µg/mL) for 48 h and then exposed to RT at varying doses, with each sample receiving a single dose of either 2.67, 4, 6, 8 and 10 Gy. Then, the cells were washed with PBS (Sigma-Aldrich, Dorset, UK), fixed with 0.25% glutaraldehyde (Sigma-Aldrich, Dorset, UK) for 20 min at room temperature and permeabilized with 0.1% Triton X (Sigma-Aldrich, Dorset, UK) for 5 min. Afterward, the cells were stained first with DAPI (Sigma-Aldrich, Dorset, UK)) and then with Phalloidin in ATTO 488 (Invitrogen; Thermo Fisher Scientific, Inc for the nuclei and actin imaging, respectively).

Morphometric quantification (coherency of F-actin) was performed on 15 cells using the OrientationJ plugin of the ImageJ 1.53a software. This parameter indicates the local orientation of actin filaments. In particular, the value of coherency ranges from 0 (isotropic orientation) to 1 (perfectly oriented structures). Nucleus circularity and nucleus-to-cytoplasm ratios were calculated by ImageJ 1.53a software.

2.9.2 Clonogenic survival assay

The clonogenic assay stands as the benchmark for assessing radiation's deleterious impact on the cellular genome [40].

Prior to analysis, 10.000 cell/petri were seeded in 8 Petri dishes of 60 x 15 mm (WillCo Wells B.V., 1054SE Amsterdam). After the delivery of X doses of radiation ranging from 0 to 10 Gy to both untreated MCF-7 cells and those treated with 0.46 µg/mL green AuNPs, cells were washed with PBS and then trypsinized for 3 min following the procedure described in [41]. Then they were resuspended in a complete medium, counted, and re-plated in 9 polystyrene petri dishes for each clonogenic test, i.e. one test for untreated cells, and two tests for treated cells. In the non-treated clonogenic assay, the cultures were sustained for 14 days, while in the treated ones, for 3 and 14 days, respectively. Afterwards, petri dishes were washed with PBS and treated with a 0.6% glutaraldehyde and 0.5% crystal violet mixture solution for 20 min. Several washes were performed with deionized water and the petri were left

to dry for 24 h at room temperature. Cellular fractional survival (SF) was calculated by a weighted, stratified, linear regression according to the linear-quadratic formula, $SF = \exp(\alpha D+\beta D^2)$.

2.9.3 Comet assay

Comet Assay is a technique used for assessing DNA damage in individual cells through gel electrophoresis [42]. Comet Assay Kit (3-Well Slides) (antibodies.com, 8 Station Court, Cambridge, CB22 5NE, United Kingdom) was used following the instructions reported in the datasheet. 4 x 10^4 MCF-7 cells were seeded onto 6-MW culture plates. After 24 h the cells were incubated with green AuNPs (0.46 µg/mL) for 48 h and then exposed to RT at varying doses, with each sample receiving a single dose of either 2.67 or 8 Gy. 24 h later the cells were scraped and resuspended (1 x 10^5 cells) in 10 µL of ice-cold PBS. The PBS aliquots were each mixed with 90 µL of 37°C low-melting point agarose and 75 µL of this solution were spread uniformly onto every well of two comet slides and left to solidify. The slides were immersed each in Lysis Buffer for 60 minutes to lyse the cells and then moved in Alkaline Solution for 30 minutes to denature the DNA. Electrophoresis was performed for 20 minutes with a voltage of 19 V and then the slides were stained with Propidium Iodide (PI). Comets were visualized by fluorescent microscopy at 20× magnification and analyzed with the ImageJ software to assess the head intensity and tail length.

2.9.4 Data analysis

Statistical analyses were performed using OriginPro (version 8.1). The difference between three and more groups was analyzed through one-way or two-way ANOVA multiple comparisons, respectively. The differences between two groups were evaluated by a two-tailed Student's-test. The differences were statistically significant when * $p < 0.05$, ** $p < 0.01$, *** $p < 0.001$).

3 Results and discussion

The application of metallic NPs as radiosensitizers in cancer therapy is garnering increasing scientific interest [43–45]. However, the specific role of green AuNPs in RT remains insufficiently investigated. The use of green AuNPs is particularly interesting since the natural capping agents used can help to reduce the toxicity of AuNPs [46], making them safer for clinical applications [47, 48]. This is particularly important for ensuring patient safety and regulatory approval. In addition, the use of readily available biological materials making lower the production costs and make the technology more accessible for widespread use [49]. For this reason, we aimed to examine the effects of these NPs in conjunction with X-ray irradiation on MCF-7 cancer cells.

Prior to expose MCF-7 cells to green AuNPs, we assessed any potential NPs alteration in terms of morphology, surface charge and size induced by X-rays delivery alone.

Then, we initially characterized by TEM the green AuNPs (Figure 3a, b). Nanostructures appeared both spherical and triangular in shape with different dimensions. The spherical ones had an average diameter of (40 ± 6) nm, while the triangular ones exhibited a larger size of about (180 ± 6) nm as reported in [37].

The crystallinity of the synthesized AuNPs was analyzed using X-ray diffraction (XRD), with the resulting XRD patterns displayed in Figure 3c. The Au nanocrystals showed four prominent peaks at 2θ values of 38.1, 44.3, 64.5, and 77.7, corresponding to the standard Bragg reflections (111), (200), (220), and (311) of a face-centered cubic (fcc) lattice structure. The strong diffraction peak at 38.1 indicated that the preferred growth direction of the zero-valent Au is oriented along the (111) plane.

This suggested that the nanocrystals form molecular-sized solids with a repeating three-dimensional arrangement of atoms or molecules, maintaining equal spacing throughout. This XRD pattern is characteristic of pure Au nanocrystals.

Then, green AuNPs were subjected to X-ray irradiation with the typical radiotherapeutic dose of 2.67 Gy (according to the protocol in Sect. 2) to evaluate any possible alterations in their physical or chemical properties. A single dose of 2.67 Gy as used, as this is the typical dose commonly employed in the RT treatment of breast cancer. The Fourier Transform Infrared (FTIR) spectroscopy was used for both non-irradiated and irradiated green AuNPs to assess any chemical change of the NPs surface. Initially, we analyzed the FTIR spectrum of the non-irradiated green AuNPs, then compared it with the spectra of both *Laurus nobilis* leaves extract and the irradiated green AuNPs. To confirm the presence of polyphenols on the NPs surface and to compare the spectra of the irradiated and non-irradiated samples, the FTIR analysis was

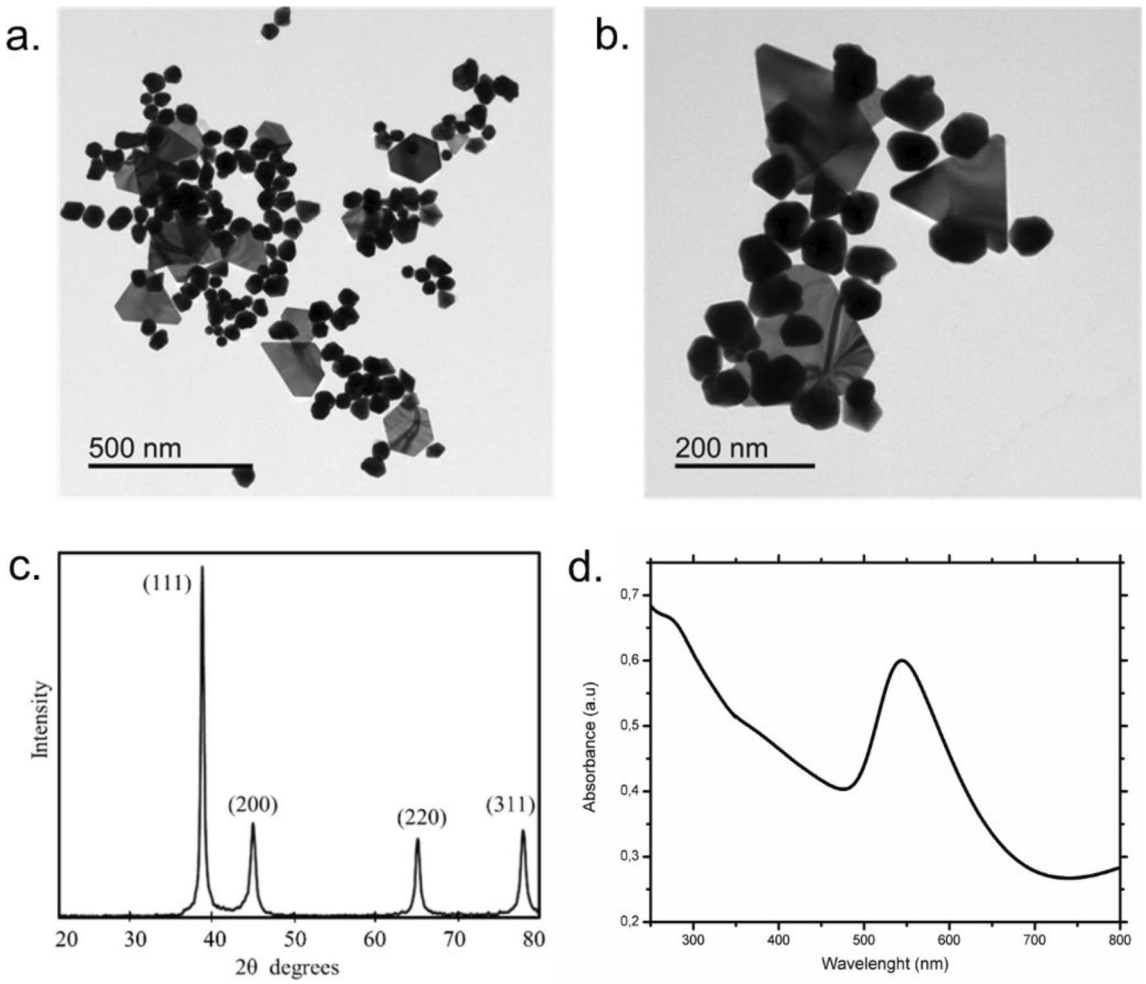

Fig. 3 Representative TEM images of green AuNPs acquired at two different magnifications **a, b**. XRD pattern **c** and UV–vis spectra **d** of green AuNPs

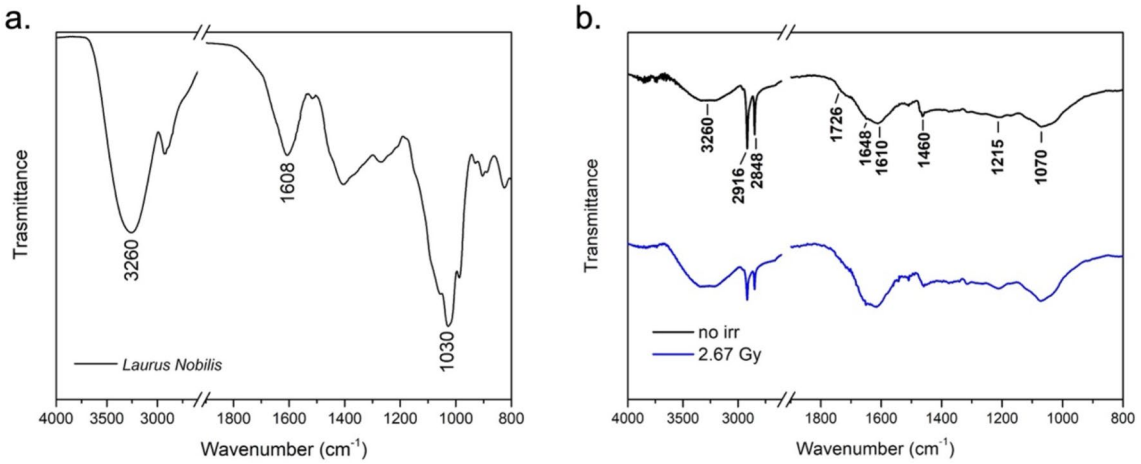

Fig. 4 ATR-FTIR spectrum of *Laurus nobilis* leaves extract **(a)**; ATR-FTIR spectra of green AuNPs before (black trace) and after 2.67 Gy (blue trace) of irradiation **(b)**

performed. For the concentration of polyphenols on AuNPs we had measured by Folin-Ciocâlteu method and reported in our previous work [37].

In Fig. 4a, b the *Laurus nobilis* leaves extract and the green AuNPs spectra were represented, respectively.

Laurus nobilis leaves contain a number of phytochemicals extracted using hot water, including saccharides, organic acids, glycosides, tannins, terpenoids, flavonoids, steroids, anthraquinones, and alkaloids [50, 51]. The ATR-FTIR spectrum of the aqueous extract, shown in Fig. 4a, presented the absorption features typical of the functional groups' characteristic of these compounds. Specifically, the intense and broad absorption band at 3260 cm^{-1} was due to O–H stretching vibration and likely arose from saccharides, phenolic compounds (tannins, flavonols, etc.), and glycosides (such as saponins). The signal centered at 1608 cm^{-1} could be ascribed to carboxylate groups from deprotonated organic acids (antisymmetric stretching vibration) as well as to stretching vibration of alkenyl C=C bonds, which could be found in terpenoids (such as sabinene and beta-pinene [52]), and some steroids, representing the aglycone moieties of saponins. Aromatic carbons from polyphenols and anthraquinones may also contribute to this broad band. The IR absorptions producing overlapped bands around 1030 cm^{-1} could be assigned to C–OH and C–O–C stretching vibrations in agreement with the presence of both saccharides and glycosidic compounds.

The ATR-FTIR spectra of green AuNPs (Fig. 4b) presented distinct features with respect to the *Laurus nobilis* aqueous extract. This indicated that specific compounds of the extract were selectively involved in NPs capping. Even though the exact identification of these compounds was not feasible by infrared spectroscopy, valuable information could be obtained about the main functional groups present in their structure. Firstly, a small shoulder was discernible around 1726 cm^{-1} indicating that chemical species bearing carbonyl groups (carboxylic acids, esters, aldehydes or ketones) are likely involved in capping. C-H stretching absorption bands at 2916 cm^{-1} and 2848 cm^{-1} are indicative of saturated alkyl chains. In addition, the signals at 1610 and 1460 cm^{-1} pointed out the presence of carboxylate moieties (antisymmetric and symmetric COO^- stretching modes) in agreement with the abundance of these functional groups in the aqueous extract. The band at 1648 cm^{-1} suggested the presence of carbon–carbon double bonds (C=C stretching), conjugated carbonyls (C=O stretching) or amine groups (N–H bending). Finally, the bands at around 1070 and 3260 cm^{-1} could be assigned to C–OH and O–H stretching vibrations respectively.

Therefore, based on the FTIR analysis, a major role played by organic acids and sugars (saccharides or glycosides) in guiding AuNPs synthesis can be proposed although the chemical complexity of the mixture employed does not exclude the involvement of further species in AuNPs decoration.

The comparison of traces in Fig. 4b showed that green NPs, whether irradiated or not, maintained an absorption pattern without differences, regardless of the intensity. This finding demonstrated that the X-ray treatment did not cause any chemical modification of the organic shell, nor an orientation change of the chemical groups directly in contact with the metal surface.

Beyond the spectroscopic assessment of the pre and post-irradiation phases, we conducted Dynamic Light Scattering (DLS) and Zeta Potential (ZP) analysis to identify any alteration in terms of size and charge of green AuNPs before and after X-rays exposure **(**Table 2**).**

Before irradiation, the NPs showed a ZP value of (−32 ± 4) mV and a hydrodynamic diameter of (45 ± 6 nm) for spherical AuNPs, and of 190 ± 5 nm for triangular AuNPs. After irradiation the ZP value became of − 30 ± 3 mV, while the hydrodynamic diameter was exactly the same for both AuNPs shapes, showing that both the charge and the size of the green AuNPs remained unchanged following X-rays exposure (data not shown). Therefore, RT did not modify the morphological properties of the green nanostructures, suggesting their potential effectiveness as radiosensitizers due to their stability.

Table 2 DLS and Zeta Potential measurements of the green AuNPs in water acquired before and after X-rays exposure

AuNPs type	Zeta potential ± SD (mV)	Hydrodynamic diameter ± SD (nm)
Pre-X-rays Irradiation		
Spherical green AuNPs	− 32 ± 4	45 ± 6
Triangular green AuNPs	− 32 ± 4	190 ± 5
Post-X-rays irradiation		
Spherical green AuNPs	− 30 ± 3	45 ± 6
Triangular green AuNPs	− 30 ± 3	190 ± 5

Table 3 The accumulation in MCF-7 cell lines exposed to nine concentrations of Au NPs@polyphenols for 48 h

AuNPs@polyphenols concentrations (μg/mL)	Au concentration (ng/mL) in cells
CTRL	0
30	10.6 ± 2
15	12.3 ± 3
7.5	12.8 ± 3
3.75	13.2 ± 5
1.9	12.2 ± 2
0.9	9.7 ± 6
0.46	4.3 ± 2
0.23	2.4 ± 3

Before performing treatments on cells using both X-rays than green AuNPs alone and in combination, cytotoxicity of green AuNPs on MCF-7 cells was assessed. For uptake, it was demonstrated that the green AuNPs showed high uptake rate in cells as reported in Table 3**.** However, the increase of uptake rate was shown when cells were exposed to 3.75 μg/mL. After this value, the uptake reaching a plateau,

The cells were then harvested, the live cells were counted, and the Au content was measured in 360,000 cells (ng Au). The control was represented by untreated cells. The data are reported as the mean of SD from three independent experiments, and statistically significantly exposed cells vs. control cells have a p value < 0.05 (< 0.05 *).

The shape of nanoparticles plays a significant role in how cells recognize, internalize, and process them. Spherical and triangular AuNPs interact with cells differently due to their geometric and physical properties. Indeed, spherical are often more easily internalized by cells through receptor-mediated endocytosis. Their symmetric shape and lower anisotropy make them more readily recognized by the cellular machinery, allowing them to follow standard endocytic pathways, such as clathrin-mediated endocytosis [53]. The triangular AuNPs possess sharper edges, and a larger surface area compared to spherical ones. This geometry enhances interactions with the cell membrane and can promote alternative uptake mechanisms, such as direct penetration or fusion with the membrane. Additionally, triangular particles may accumulate more efficiently in specific cellular compartments, like the lysosomes, due to their due to their unique shape [54, 55]. Then, combining spherical and triangular nanoparticles could have a synergistic effect on cellular uptake. While spherical NPs are quickly absorbed via conventional endocytic processes, triangular nanoparticles can interact differently with the cell membrane, facilitating uptake through alternate pathways. This diversity in uptake mechanisms could potentially increase the overall rate of nanoparticle internalization [55, 56]. The spherical AuNPs are efficiently internalized via clathrin-mediated endocytosis, rapidly accumulating within cells and enhancing the radiation dose that reaches the tumor. Triangular AuNPs, due to their sharp edges and larger surface area, can interact with the cell membrane more effectively, penetrating through alternative mechanisms and reaching subcellular compartments that spherical particles might not access. These triangular NPs can localize in areas where radiation effects can be maximized, such as in the lysosomes or cytosol [37, 54].

Cell viability was assessed on three groups of cells: non-irradiated MCF-7 treated with varying concentrations of green AuNPs (0, 0.23, 0.46, 0.9, 1.8, 3.7, 7.5, 15 and 30 μg/mL); CTRL MCF-7 s (untreated) irradiated at different radiation doses (0, 2.67, 4, 6, 8 and 10 Gy); and MCF-7 s both incubated with green AuNPs (0, 0.23, 0.46, 0.9, 1.8, 3.7, 7.5, 15 and 30 μg/mL) and irradiated (0, 2.67, 4, 6, 8 and 10 Gy). In Fig. 5a, b and in Fig. 6 all the results were reported.

As illustrated in Fig. 5a, MCF-7 s were incubated with different concentrations of green AuNPs (0.23, 0.46, 0.9, 1.8, 3.7, 7.5, 15 and 30 μg/mL), without RT exposure. After 72 h of incubation period cell viability was assessed. The incubation alone did not cause any cytotoxic effect towards the tumor cells, indicating the biocompatibility of green AuNPs probably due to their natural plants derivation and polyphenols/fitomolecules shell [57].

For cells without green AuNPs, the effect of different RT doses (2.67, 4, 6, 8, and 10 Gy) is reported in Fig. 5b. Specifically, irradiation was performed 48 h after seeding, followed by MTT analysis 24 h post-irradiation, consistently maintaining a 72-h incubation period prior to analysis. Cell viability significantly decreased statistically in a RT dose-dependent manner by up to 40% at 10 Gy, just as expected from the typical therapeutic action of RT alone.

The cytotoxic effect of green AuNPs towards MCF-7 when exposed to RT was depicted in Fig. 6; MCF-7 were incubated with increasing green AuNPs concentrations (0.23, 0.46, 0.9, 1.8, 3.7, 7.5, 15 and 30 μg/mL) and after 48 h the cells were

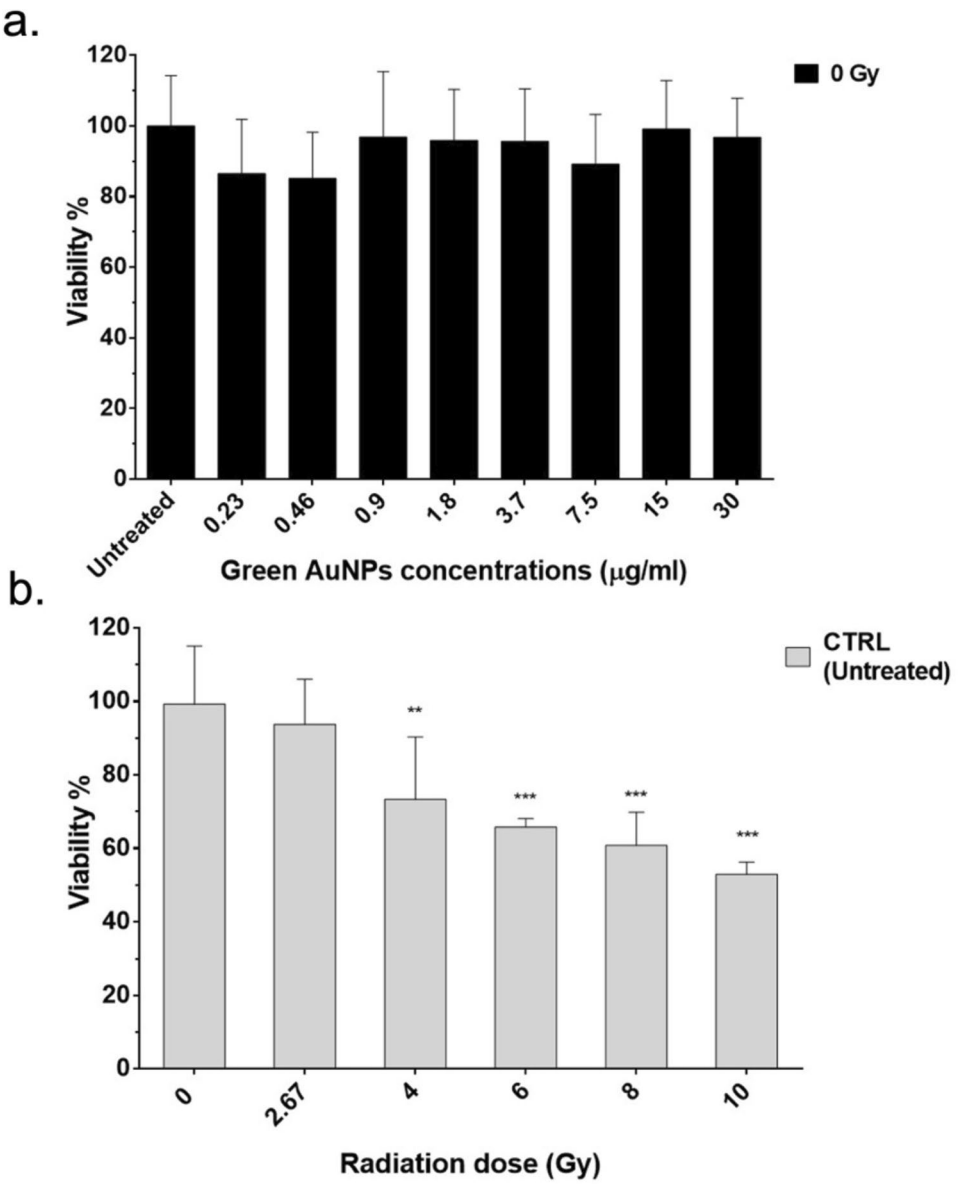

Fig. 5 **a** Percentage of viability of non-irradiated MCF-7 cells treated with different concentrations of green AuNPs (0.23, 0.46, 0.9, 1.8, 3.7, 7.5, 15 and 30 µg/mL) for 72 h**.** Cytotoxic activity for each sample was normalized to the CTRL (untreated) cells represented by the first column of the bar graph. **b** Percentage of viability for CTRL (untreated) MCF-7 cells irradiated with various radiation doses (2.67, 4, 6, 8 and 10 Gy) 48 h after seeding and analyzed 24 h post- irradiation, resulting in a total incubation period of 72 h. Cytotoxic activity for each sample was normalized to the CTRL (untreated) cells represented by the first column of the bar graph

exposed to varying radiation dose ranging from 2.67 to 10 Gy. After an additional 24 h post-irradiation, MCF-7 cells were analyzed using MTT assay, ensuring the same total incubation period of 72 h. Each data was normalized on the CTRL (untreated) sample, placed as a reference on the y-axis at 100% cell viability (black dashed line). In this MTT analysis, for how concerned cells irradiated with 2.67 Gy, only the concentration of 15 µg/mL green AuNPs resulted in a statistically significant reduction in cell viability. For all other X-rays doses (4, 6, 8 and 10 Gy), MCF-7 viability decreased by 30% to 50% across all AuNPs concentrations (0.23, 0.46, 0.9, 1.8, 3.7, 7.5, 15 and 30 µg/mL), resulting in statistically significant cell viability reductions in every scenario.

After thoroughly evaluating the effects of various concentrations of green AuNPs, we identified 0.46 µg/mL as the optimal choice for further testing. This concentration was the most statistically significant in reducing cellular metabolic activity across both high and low radiation doses. In contrast, higher concentrations of green AuNPs appeared to slightly enhance cell viability despite X-ray irradiation. This unexpected result is likely due to the anti-inflammatory properties of the polyphenol shell, which, at these elevated concentrations, not only mitigated toxicity [39]. but also provided protective effects on MCF-7 cells. This effect was demonstrated in vivo and in vitro in some publications [58–60].

The dual nature of polyphenols adds a significant layer of complexity to the interpretation of our results, particularly in the context of their radiosensitizing effects. Indeed, the apparent contradiction between the antioxidant role of polyphenols and their contribution to the radiosensitization observed. This dual functionality suggests that, while

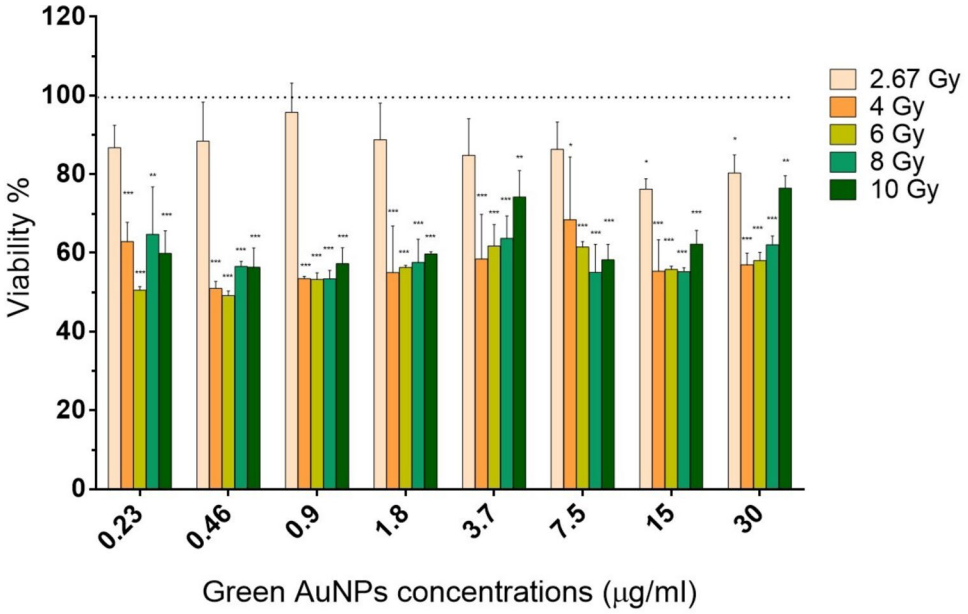

Fig. 6 Viability of MCF-7 cells incubated with different concentrations of green AuNPs (0.23, 0.46, 0.9, 1.8, 3.7, 7.5, 15 and 30 μg/mL), followed by irradiation with varying doses (2.67, 4, 6, 8 and 10 Gy) 48 h after incubation and analyzed with MTT assay 24 h post-irradiation, for a total incubation period of 72 h. All data were normalized on the CTRL (untreated) sample, indicated on the y-axis by the percentage viability reference value of 100% (black dashed line)

polyphenols can reduce toxic effects under certain conditions, their behavior may shift when they are immobilized on the surface of metal nanoparticles. This shift could be due to changes in their redox environment or interactions with cellular components, which may lead to the generation of redox species instead of their neutralization, especially under radiation exposure.

The capability to modify cell morphology in terms of actin fibers was investigated by confocal analysis. Analyzing the modifications of actin fibers induced by NPs and RT in cancer cells is crucial for several reasons. Actin fibers play a fundamental role in maintaining the structural integrity, motility, and division of cells. Any alterations in the organization or dynamics of these fibers can significantly impact cellular behavior, potentially leading to changes in cell adhesion, migration, and invasion—key processes in cancer progression and metastasis [61]. Understanding how NPs and RT interact with and modify actin fibers can provide insights into their mechanisms of action, reveal potential therapeutic benefits, and help in designing more effective and targeted cancer treatments. guiding the safe and effective use of NPs in clinical settings.

The effects of radiation on MCF-7, with and without green AuNPs, were collected in Fig. 7. We used two X-rays doses, i.e. 2.67 Gy, the therapeutic dose, and 8 Gy to test a high radiation dose.

As revealed by acquisitions **(a)** and **(b)** in Fig. 7, the non-irradiated MCF-7 cells, whether alone (Fig. 7a) or incubated with a 0.46 μg/mL concentration of green AuNPs (Fig. 7b**)**, showed no alteration in cortical actin that appear organized in fibers with the same orientation. By contrast, in the presence of radiation alone (Fig. 7c,e), the alteration of actin fibers was greater than in the non-irradiated cells. Specifically, in the MCF-7 cells irradiated with 2.67 Gy and 8 Gy, respectively, showed alteration in cortical actin pattern that was more evident at 8 Gy. Cell damage, however, was even more significant than RT alone when MCF-7 s were incubated with 0.46 μg/mL-concentration green AuNPs and then irradiated at 2.67 Gy (Fig. 7d) and 8 Gy (Fig. 7f), respectively. In the latter cases, the synergistic effects of X-rays and green AuNPs. The synergistic action of RT and NPs results in increased disorganization of actin fibers. Indeed, they appear curled, and the cells begin to lose their cellular junctions. The confocal-acquired images were then analyzed by ImageJ to assess the coherency of actin fibers, i.e. their degree of organization.

This value is dimensionless and ranges from 0 to 1. A value near 1 indicates organized fibers, while a value tending more toward 0 indicates a high degree of disorganization. In addition, we performed the assessment of nuclei morphometric parameters since the deformation of nucleus in terms of circularity is an index of induced stress on breast cancer cells. Indeed, alteration in nuclear shape is a distinct feature of malignancy associated to DNA damage [62]. For circularity, value of 1 represents a perfect circle and 0 represents a straight line. In addition to examining cytoskeletal rearrangements and nuclei shape, we also assessed the area represented by the nucleus-to-cytoplasm ratio. The Nucleus/cytoplasm ratio was determined by calculating the ratio of the nuclear area to the total cellular area. The increase in the nucleus-to-cytoplasm ratio following radiation exposure can be attributed to a combination of cytoplasmic damage and alterations, nuclear expansion, cell cycle modifications, and cellular stress responses. These changes reflect the cell's

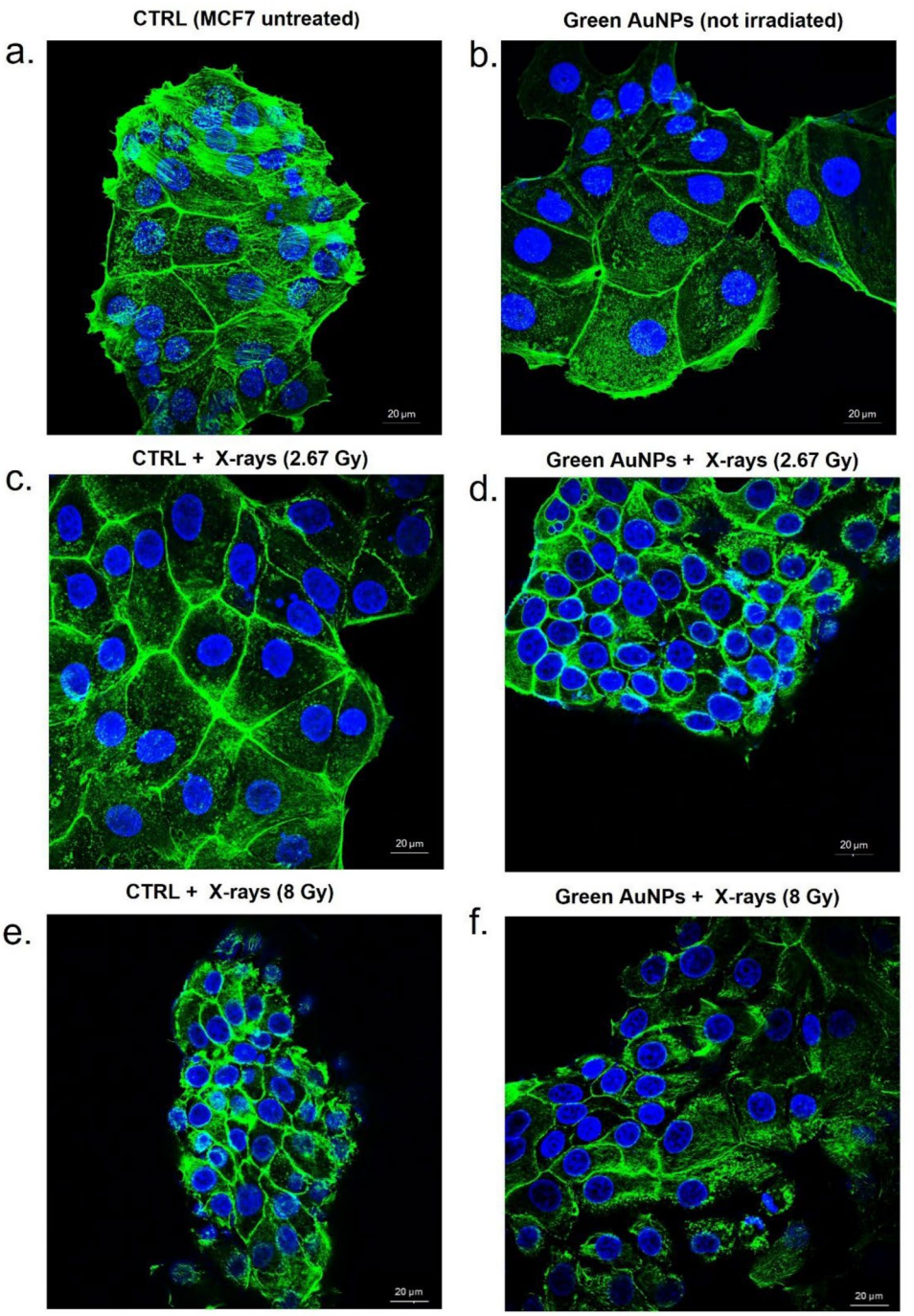

Fig. 7 Confocal images of actin fibers (green) and nuclei (blue) of MCF-7 cells acquired under different conditions: **a** CTRL (MCF-7 untreated); **b** MCF-7 incubated with green AuNPs (0.46 µg/mL) (not irradiated); **c** CTRL irradiated with 2.67 Gy X-rays dose; **d** MCF-7 incubated with green AuNPs (0.46 µg/mL) and irradiated with 2.67 Gy X-rays dose; **e** CTRL irradiated with 8 Gy X-rays dose; **f** MCF-7 incubated with green AuNPs (0.46 µg/mL) and irradiated with 8 Gy X-rays dose

reaction to the damage and its ability to repair or respond to such damage. Starting from these assumptions in Fig. 8a,b,c the analyses of actin coherency, nucleus circularity and nucleus to cytoplasm ratio, were displayed.

Regarding actin coherency, normally, in healthy cells filaments appears helical in shape [63] and relatively well-organized, particularly when referring to cortical actin. However, when cells were irradiated, or in general subjected to a process causing biological damage, the actin filaments became disorganized and disintegrated, resulting in lower coherency value [64]. In our work, MCF-7 cells exhibited X-rays dose-dependent statistically significant loss of coherency (Fig. 8a), whether alone or incubated with a 0.46 µg/mL concentration of green AuNPs. However, the most noticeable reduction was obtained in cells treated with 0.46 µg/mL green AuNPs and irradiated with 2.67 and 8 Gy.

As for the nuclei circularity (Fig. 8b), it was close to the value 0 if the nucleus was highly deformed, otherwise, the value is near to 1, when nucleus is perfectly circular. MCF-7 nuclei showed a significant reduction in circularity in an

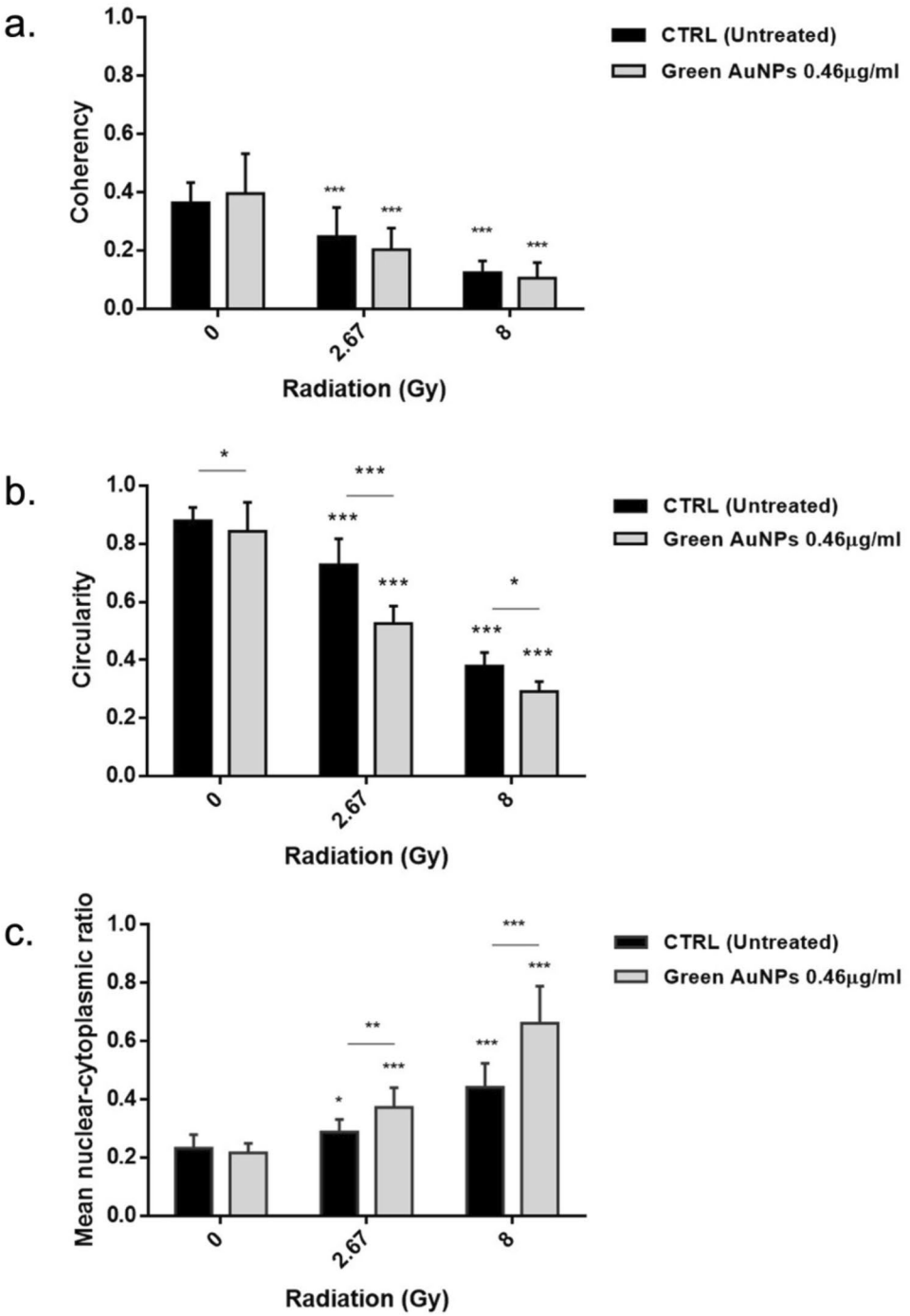

Fig. 8 Analysis of actin coherency **a**; nucleus circularity **b** and nucleus to cytoplasm ratio of MCF-7 cells **c** performed on 30 cells

X-rays dose dependent manner, both when incubated with 0.46 µg/mL green AuNPs and in their absence. However, the growing nucleus deformity was amplified by the 0.46 µg/mL green AuNPs incubation. In the irradiated cells, i.e. without green AuNPs, the circularity decreased until 0.7 and 0.4 values using doses of 2.67 and 8 Gy, respectively, compared with the unirradiated value of 0.9. In the green AuNPs-incubated cells irradiated with 2.67 and 8 Gy, the reduction in nucleus circularity declined by up to 0.5 and 0.3, respectively, proving how the synergistic effect of green AuNPs and X-rays further promoted biological damage to cancer cells. All *p*-value tests between the irradiated sample and the respective control were fulfilling, with more statistically significant results for the AuNPs-treated samples.

The nucleus-to-cytoplasm ratio is another important factor regarding cell integrity. In an uninjured cell, the cytoplasm, consisting of microtubules, intermediate filaments and F-actin filaments [65], occupies about half of the total

volume, while the nucleus occupies a smaller portion [66]. In contrast, in a damaged cell, the nucleus to cytoplasm ratio tends to increase due to the disintegration of the cytoplasm [67]. We analyzed the nucleus to cytoplasm ratio of different MCF-7 cells that received 0, 2.67 and 8 Gy of X-ray radiation, in both samples with and without 0.46 µg/mL green AuNPs concentration (Fig. 8c).

In the irradiated samples not treated with green AuNPs, the nucleus-to-cytoplasm ratio increased with higher radiation doses. Specifically, the CTRL (untreated) and non-irradiated sample (0 Gy) had a nucleus to cytoplasm value of 0.2. In contrast, the CTRL (untreated) irradiated with doses of 2.67 and 8 Gy exhibited nucleus-to-cytoplasm ratios of 0.3 and 0.4, respectively. The increase in this ratio was notably more pronounced in irradiated MCF-7 cells that were incubated with 0.46 µg/mL-concentration green AuNPs. For these cells, the nucleus-to-cytoplasm ratio reached the value of 0.4 following irradiation and 0.7 following irradiation with 8 Gy. These results clearly indicated that cells treated with 0.46 µg/mL-green AuNPs concentration and irradiated at different doses, experienced significant disintegration of their cellular structure, particularly the cytoplasm, leaving meanly the deformed nucleus.

The cells' ability to form colonies after the delivery of X-rays doses was analyzed using the clonogenic assay. Clonogenic survival is the most widely used biological test to assess variations in cell survival following irradiation [68] both in treated and untreated samples. In our work clonogenic assay was performed on different groups: Control MCF-7 (untreated) irradiated with doses ranging from 2.67 to 10 Gy and stained after 14 days; MCF-7 incubated with 0.46 µg/mL green AuNPs, irradiated, and immediately stained after 3 days; and MCF-7 cells incubated with 0.46 µg/mL green AuNPs, irradiated, and stained after a delay of 14 days.

Figure 9g, h vividly illustrated the dose–response curves for MCF-7 cells, both with and without incubation with 0.46 µg/mL green AuNPs, across a range of radiation doses from 2.67 to 10 Gy. Notably, Fig. 9g showed that MCF-7 cells incubated with 0.46 µg/mL green AuNPs, irradiated 48 h post incubation and stained 14 days later (●) exhibited a significant lower survival rate compared to those stained after just 3 days (△). This difference was evident even at low radiation doses, indicating that prolonged incubation with green AuNPs markedly decreased cell survival. Similarly, Fig. 9h compared two scenarios: CTRL (untreated) MCF-7 cells irradiated 48 h after seeding and stained 14 days post-irradiation (×), and MCF-7 incubated with 0.46 µg/mL green AuNPs, irradiated 48 h post-incubation and stained 14 days post-irradiation (●). The survival fraction of cells incubated with green AuNPs was lower than that of the non-incubated ones, with both

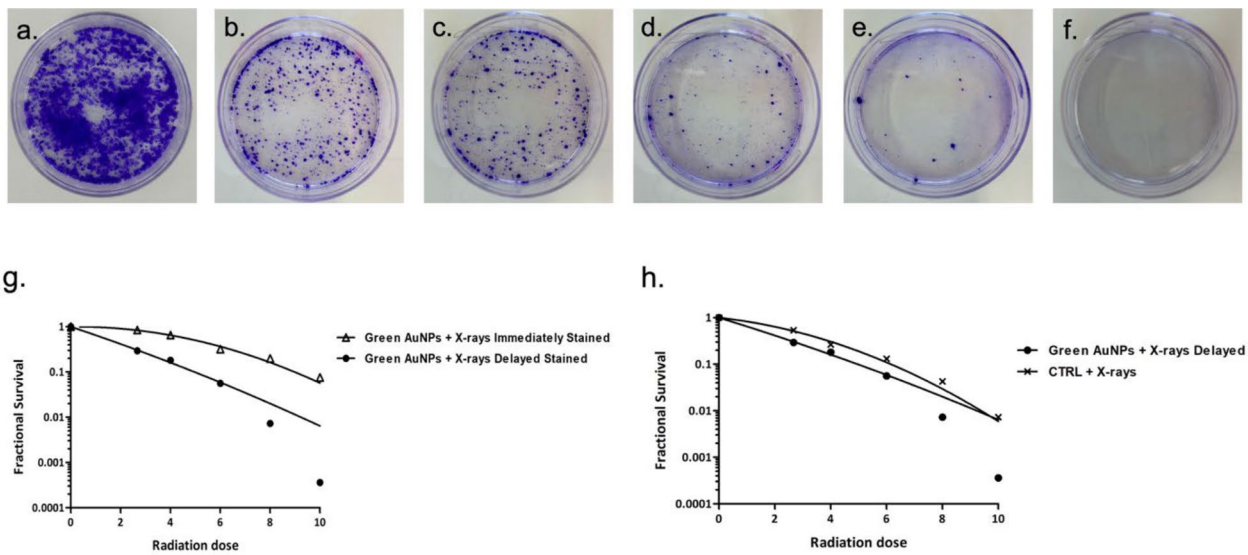

Fig. 9 **a–f**, Petri dishes from the clonogenic assay of MCF-7 cells incubated with 0.46 µg/mL green AuNPs, irradiated and stained after 14 days. The irradiations corresponded to: **a** CTRL MCF-7 (untreated) not irradiated, **b** 2.67 Gy of X-rays dose, **c** 4 Gy of X-rays dose, **d** 6 Gy of X-rays dose, **e)** 8 Gy of X-rays dose, **f** 10 Gy of X-rays dose. **g** (△) Survival curves of MCF-7 incubated with 0.46 µg/mL green AuNPs concentration, irradiated with doses ranging from 2.67 to 10 Gy after 48 h from incubation, and immediately stained after 3 days post-irradiation ($y = -0.0869\ x^2 - 0.094\ x$; $R^2 = 0.9944$); (●) survival curves of MCF-7 incubated with 0.46 µg/mL green AuNPs concentration, irradiated with doses ranging from 2.67 to 10 Gy after 48 h from incubation, and delayed stained after 14 days post-irradiation ($y = -0.0973\ x^2 - 0.3236\ x$; $R^2 = 0.9547$). **h)** (●) Survival curves of MCF-7 incubated with 0.46 µg/mL green AuNPs concentration, irradiated with doses ranging from 2.67 to 10 Gy after 48 h from incubation, and delayed stained after 14 days post-irradiation ($y = -0.0973\ x^2 - 0.3236\ x$; $R^2 = 0.9547$); (×) survival curve of CTRL MCF-7 (untreated) irradiated with doses ranging from 2.67 to 10 Gy after 48 h from seeding, and stained after 14 days post-irradiation ($y = -0.0256\ x^2 - 0.2391\ x$; $R^2 = 0.9919$).

survival curves converging at higher radiation doses, specifically from 6 Gy and above. Among the various experiments conducted, MCF-7 cells incubated with green AuNPs for an extended period showed a significant reduction in survival across all radiation doses. At higher doses (ranging from 6 to 10 Gy), the survival curves converged, likely due to cumulative radiation damage. This trend indicated that prolonged incubation with green AuNPs enhanced the radiosensitivity of MCF-7 cells, thereby amplifying the cytotoxic effects of radiation (Fig. 9a–f).

At this point, we investigated whether the morphological changes in the cells, particularly in the nuclei, were consistent with potential DNA damage. The loss of circularity in the nuclei of MCF-7 cells subjected to treatment indicates damage to the nuclear lamina. However, to confirm actual DNA damage in the form of single or double-strand breaks, we performed the Comet Assay also known as single-cell gel electrophoresis.

The comet assay is a widely validated method for detecting single-strand breaks and, in this context, has provided significant insights into DNA damage, despite not being able to fully detect complex damages. Inducing DNA damage is crucial in combined anti-tumor therapy. However, such treatments often damage healthy cells as well. The use of AuNPs, precisely confined to the tumor site, could significantly reduce this risk. In Fig. 10a–f representative images of cells were reported following the treatments described in the above experiments. the comet morphology was observed only in cells treated with X-rays and green AuNPs incubating for 48 h. Although the analysis at a single time point limits the understanding of the dynamic effects of damage and repair, our results still provide a solid foundation for future explorations. Furthermore, a time point coinciding with the peak of the effect may be the most relevant window for the initial analysis of DNA damage, effectively limiting the impact of this limitation.

Consistently, the greater tail length, corresponding to greater DNA damage, was primarily visible in cells irradiated with X-rays that have previously internalized green AuNPs. By performing image analysis with ImageJ, it was possible to evaluate the head intensity and tail length, with data reported in Fig. 10g and h. The control group shows higher head intensity percentages (Fig. 10h), indicating that the genetic material remains intact within the nucleus. In this sense, only the CTRLs not treated with radiation and green AuNPs and MCF-7 cells incubated with only green AuNPs (0.46 µg/mL) exhibited a higher head intensity percentage, i.e., 70% ± 5 and 64% ± 3 respectively. In contrast, cells treated with green AuNPs and X-rays at 2.67 Gy and 8 Gy have tail lengths of 52 µm and 63 µm, respectively (Fig. 10g). In preliminary studies like ours, a sample size of this type is perfectly acceptable, and the obtained data are already statistically significant.

4 Conclusions

In our groundbreaking work, we have harnessed the potential of AuNPs synthesized from plant extracts as potent enhancers of radiotherapy in breast cancer cells. This topic is particularly compelling given the widespread use of X-rays in cancer treatment, often in combination with other therapies. While numerous studies explore the unique physicochemical properties of AuNPs in conjunction with radiotherapy, our research stands out as one of the few to utilize stable, well-characterized green multishaped AuNPs with high yield, making them viable candidates for clinical applications. The combined use of spherical and triangular AuNPs in radiotherapy presents a promising approach to enhancing cancer treatment. Their distinct uptake mechanisms and the additional benefit of plasmonic photothermal effects make them powerful radiosensitizers. This synergistic effect can lead to more effective cancer cell destruction while minimizing damage to healthy tissue. Therefore, utilizing these shapes in combination with radiotherapy represents a significant advancement in nanoparticle-based cancer therapies. The green AuNPs we employed have demonstrated remarkable biocompatibility in the absence of irradiation. However, when combined with therapeutic doses of X-rays, these nanoparticles transform into toxic agents capable of destroying DNA, altering cellular morphology, inhibiting colony formation, and significantly reducing cell viability. This dual behavior underscores their potential as powerful radiosensitizers. Indeed, the combined use of spherical and triangular AuNPs induce a synergistic effect that can lead to more effective cancer cell destruction while minimizing damage to healthy tissue enhancing the efficacy of radiotherapy. While further in vivo studies are needed to fully understand their biodistribution and long-term effects, the initial findings are highly encouraging. This innovative approach not only leverages the biocompatibility and stability of plant-derived nanoparticles but also paves the way for more effective and targeted cancer therapies in the future potentially offering new hope to patients worldwide.

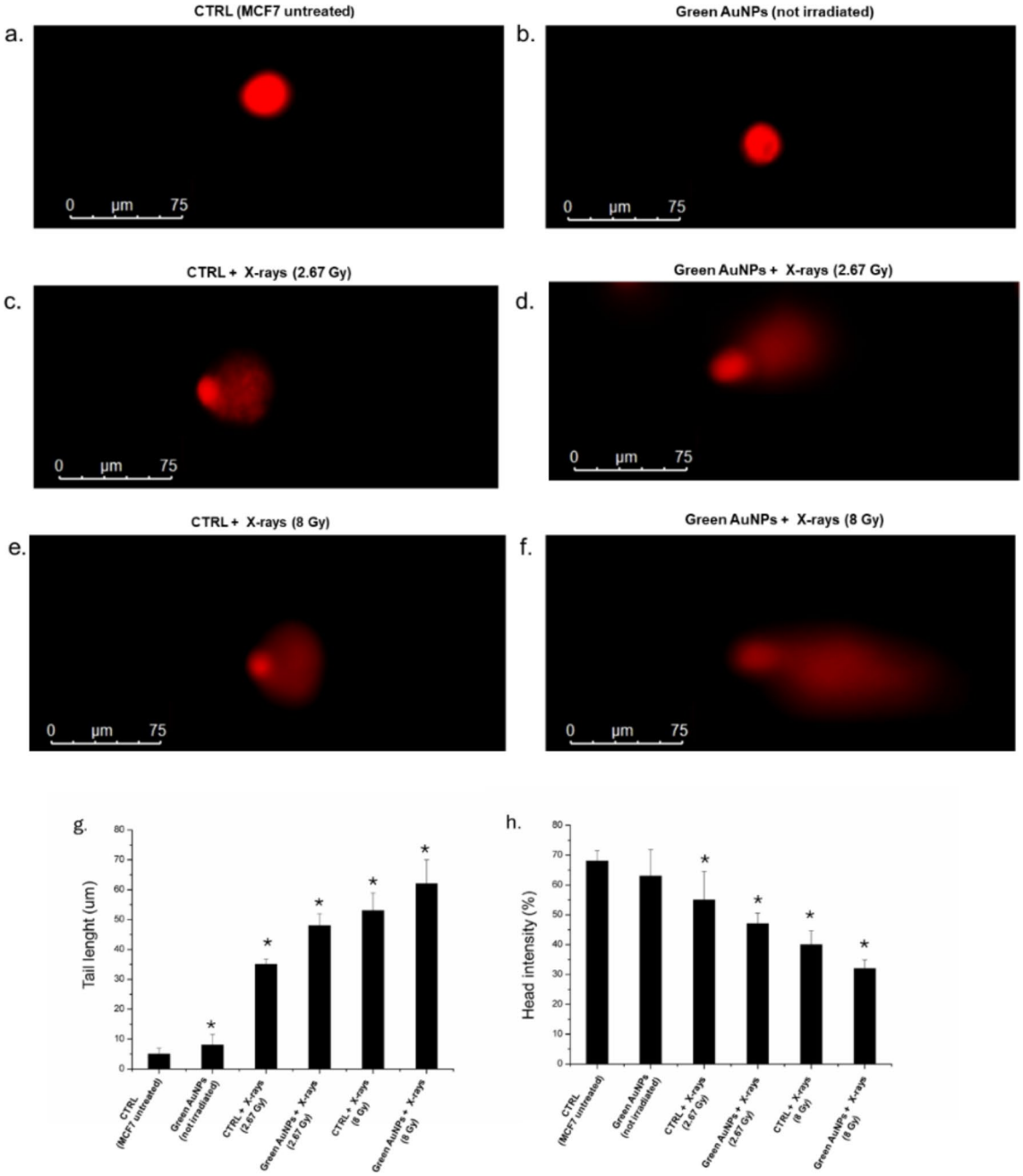

Fig. 10 Representative images of X-rays and green AuNPs on DNA damage in MCF-7 obtained by comet assay **a** CTRL (MCF-7 untreated); **b** MCF-7 incubated with green AuNPs (0.46 µg/mL) (not irradiated); **c** CTRL irradiated with 2.67 Gy X-rays dose; **d** MCF-7 incubated with green AuNPs (0.46 µg/mL) and irradiated with 2.67 Gy X-rays dose; **e** CTRL irradiated with 8 Gy X-rays dose; **f** MCF-7 incubated with green AuNPs (0.46 µg/mL) and irradiated with 8 Gy X-rays dose. DNA damage was evaluated by g tail length (µm) and h head intensity (%). Values shown are means from 100 randomly selected comet images of each sample. As positive control (P) cells were incubated with 500 µM H_2O_2 (data not shown). Data are reported as mean ± SD from three independent experiments; *$p < 0.05$ compared with control (MCF-7 untreated) ($n = 3$)

Acknowledgements S.T. kindly acknowledges PON R&I azione innovazione- F85F21005870001 entitled: "Functionalized gold nanoparticles (AuNPs) to support radiotherapy treatments of radioresistant tumors" for sponsoring her PhD fellowship program. M.C. kindly acknowledges PRP@CERIC-CUP J97G22000400006 for sponsoring her salary and work. V.D.M. kindly acknowledges Programma Operativo Nazionale (PON) Ricerca e Innovazione 2014–2020-Azione IV.6 "Contratti su tematiche green"-DM 1062/2021 for sponsoring her salary and work.

Author contributions V.D.M. conceived the idea of the manuscript; S.T. and V.D.M. synthesized the nanomaterials; A.C. and L.F. performed the irradiation experiments; S.T., V.D.M., R.D.C, L.G. characterized the nanomaterials and performed the data analysis; S.T, V.D.M, M.F.C, A.B., P.P. performed biological experiments; A.P.C., R.R. and V.D.M. supervised the work; S.T. and A.B. wrote the draft of manuscript. All authors edited the manuscript and agreed to the published version of the manuscript.

Data availability Data is provided within the manuscript.

Declarations

Competing interests The authors declare no competing interests.

Bibliographys

1. Ghoncheh M, Pournamdar Z, Salehiniya H. Incidence and mortality and epidemiology of breast cancer in the world. Asian Pac J Cancer Prev. 2016;17(sup3):43–6. https://doi.org/10.7314/APJCP.2016.17.S3.43.
2. Baskar R, Lee KA, Yeo R, Yeoh K-W. Cancer and radiation therapy: current advances and future directions. Int J Med Sci. 2012;9(3):193–9. https://doi.org/10.7150/ijms.3635.
3. Bartsch R, et al. Ovarian function suppression and fulvestrant as endocrine therapy in premenopausal women with metastatic breast cancer. Eur J Cancer. 2012;48(13):1932–8. https://doi.org/10.1016/j.ejca.2012.03.002.
4. Chan A, et al. Neratinib after trastuzumab-based adjuvant therapy in patients with HER2-positive breast cancer (ExteNET): a multicentre, randomised, double-blind, placebo-controlled, phase 3 trial. Lancet Oncol. 2016;17(3):367–77. https://doi.org/10.1016/S1470-2045(15)00551-3.
5. Hung S-K, et al. Molecular subtypes of breast cancer predicting clinical benefits of radiotherapy after breast-conserving surgery: a propensity-score-matched cohort study. Breast Cancer Res. 2023;25(1):149. https://doi.org/10.1186/s13058-023-01747-9.
6. Kargozar S, Mozafari M. Nanotechnology and nanomedicine: start small, think big. Mater Today Proc. 2018;5(7):15492–500. https://doi.org/10.1016/j.matpr.2018.04.155.
7. Sindhwani S, Chan WCW. Nanotechnology for modern medicine: next step towards clinical translation. J Intern Med. 2021;290(3):486–98. https://doi.org/10.1111/joim.13254.
8. Jurj A, Braicu C, Pop L-A, Tomuleasa C, Gherman C, Berindan-Neagoe I. The new era of nanotechnology, an alternative to change cancer treatment. DDDT. 2017;11:2871–90. https://doi.org/10.2147/DDDT.S142337.
9. Tarantino S, Caricato AP, Rinaldi R, Capomolla C, De Matteis V. Cancer treatment using different shapes of gold-based nanomaterials in combination with conventional physical techniques. Pharmaceutics. 2023;15(2):500. https://doi.org/10.3390/pharmaceutics15020500.
10. Nagi NMS, Khair YAM, Abdalla AME. Capacity of gold nanoparticles in cancer radiotherapy. Jpn J Radiol. 2017;35(10):555–61. https://doi.org/10.1007/s11604-017-0671-6.
11. Her S, Jaffray DA, Allen C. Gold nanoparticles for applications in cancer radiotherapy: mechanisms and recent advancements. Adv Drug Deliv Rev. 2017;109:84–101. https://doi.org/10.1016/j.addr.2015.12.012.
12. Chen Y, Yang J, Fu S, Wu J. Gold nanoparticles as radiosensitizers in cancer radiotherapy. Int J Nanomed. 2020;15:9407–30. https://doi.org/10.2147/IJN.S272902.
13. Penninckx S, Heuskin A-C, Michiels C, Lucas S. The role of thioredoxin reductase in gold nanoparticle radiosensitization effects. Nanomedicine. 2018;13(22):2917–37. https://doi.org/10.2217/nnm-2018-0171.
14. Mohammadi F, Soltani A, Ghahremanloo A, Javid H, Hashemy SI. The thioredoxin system and cancer therapy: a review. Cancer Chemother Pharmacol. 2019;84(5):925–35. https://doi.org/10.1007/s00280-019-03912-4.
15. Penninckx S, Heuskin A-C, Michiels C, Lucas S. Thioredoxin reductase activity predicts gold nanoparticle radiosensitization effect. Nanomaterials. 2019;9(2):295. https://doi.org/10.3390/nano9020295.
16. Wu P-H, et al. Targeting integrins with RGD-conjugated gold nanoparticles in radiotherapy decreases the invasive activity of breast cancer cells. IJN. 2017;12:5069–85. https://doi.org/10.2147/IJN.S137833.
17. S. Teraoka *et al.*, 'Gold nanoparticles enhance X-ray irradiation-induced apoptosis in head and neck squamous cell carcinoma in vitro', *biom rep*, Aug. 2018, https://doi.org/10.3892/br.2018.1142.
18. Rahman WN, et al. 'Enhancement of radiation effects by gold nanoparticles for superficial radiation therapy.' Nanomed Nanotechnol Biol Med. 2009;5(2):136–42. https://doi.org/10.1016/j.nano.2009.01.014.
19. Mulgaonkar A, Moeendarbari S, Silvers W, Hassan G, Sun X, Hao Y, Mao W. Hollow gold nanoparticles as efficient in vivo radiosensitizing agents for radiation therapy of breast cancer. J Biomed Nanotechnol. 2017;13(5):566–74. https://doi.org/10.1166/jbn.2017.2367.

20. Sato T, et al. Gold nanoparticles enhance the tumor growth-suppressing effects of cetuximab and radiotherapy in head and neck cancer in vitro and in vivo. Cancers. 2023;15(23):5697. https://doi.org/10.3390/cancers15235697.
21. Singh P, Pandit S, Mokkapati VRSS, Garg A, Ravikumar V, Mijakovic I. Gold nanoparticles in diagnostics and therapeutics for human cancer. IJMS. 2018;19(7):1979. https://doi.org/10.3390/ijms19071979.
22. Patil S, Chandrasekaran R. Biogenic nanoparticles: a comprehensive perspective in synthesis, characterization, application and its challenges. J Genetic Eng Biotechnol. 2020;18(1):67. https://doi.org/10.1186/s43141-020-00081-3.
23. Pandit C, et al. Biological agents for synthesis of nanoparticles and their applications. J King Saud Univ Sci. 2022;34(3): 101869. https://doi.org/10.1016/j.jksus.2022.101869.
24. Ahmed S, Ikram S. Biosynthesis of gold nanoparticles: a green approach. J Photochem Photobiol B Biol. 2016;1(161):141–53. https://doi.org/10.1016/j.jphotobiol.2016.04.034.
25. Dobroslavić E, Elez Garofulić I, Zorić Z, Pedisić S, Dragović-Uzelac V. Polyphenolic characterization and antioxidant capacity of *Laurus nobilis* L. leaf extracts obtained by green and conventional extraction techniques. Processes. 2021;9(10):1840. https://doi.org/10.3390/pr9101840.
26. Dobroslavić E, Repajić M, Dragović-Uzelac V, Elez GI. Isolation of *Laurus nobilis* leaf polyphenols: a review on current techniques and future perspectives. Foods. 2022;11(2):235.
27. Mohammadzadeh V, et al. Applications of plant-based nanoparticles in nanomedicine: a review. Sustain Chem Pharm. 2022;25: 100606. https://doi.org/10.1016/j.scp.2022.100606.
28. Adeyemi JO, Oriola AO, Onwudiwe DC, Oyedeji AO. Plant extracts mediated metal-based nanoparticles: synthesis and biological applications. Biomolecules. 2022;12(5):627. https://doi.org/10.3390/biom12050627.
29. Akintelu SA, Yao B, Folorunso AS. Green synthesis, characterization, and antibacterial investigation of synthesized gold nanoparticles (AuNPs) from Garcinia kola pulp extract. Plasmonics. 2021;16(1):157–65. https://doi.org/10.1007/s11468-020-01274-9.
30. Ahmed I, Mir FA, Banday JA. Synthesis of metal and metal oxide nanoparticles using plant extracts—characterization and applications. BioNanoSci. 2023;13(4):1541–57. https://doi.org/10.1007/s12668-023-01194-y.
31. Bharadwaj KK, et al. Green synthesis of gold nanoparticles using plant extracts as beneficial prospect for cancer theranostics. Molecules. 2021;26(21):6389. https://doi.org/10.3390/molecules26216389.
32. Nadaf SJ, et al. Green synthesis of gold and silver nanoparticles: updates on research, patents, and future prospects. OpenNano. 2022;8: 100076. https://doi.org/10.1016/j.onano.2022.100076.
33. Phan TTV, Nguyen VT, Ahn S-H, Oh J. Chitosan-mediated facile green synthesis of size-controllable gold nanostars for effective photothermal therapy and photoacoustic imaging. Eur Polymer J. 2019;118:492–501. https://doi.org/10.1016/j.eurpolymj.2019.06.023.
34. Ferreira-Gonçalves T, et al. The role of rosmarinic acid on the bioproduction of gold nanoparticles as part of a photothermal approach for breast cancer treatment. Biomolecules. 2022;12(1):71. https://doi.org/10.3390/biom12010071.
35. Silva CO, et al. Bioproduction of gold nanoparticles for photothermal therapy. Ther Deliv. 2016;7(5):287–304. https://doi.org/10.4155/tde-2015-0011.
36. R. Reilly, 'Breast Cancer', in *xPharm: The Comprehensive Pharmacology Reference*, Elsevier, 2007, pp. 1–9. https://doi.org/10.1016/B978-008055232-3.60809-8.
37. De Matteis V, et al. Multishaped bio-gold polyphenols bearing nanoparticles to promote inflammatory suppression. Nano Today. 2024;57: 102329. https://doi.org/10.1016/j.nantod.2024.102329.
38. Tarantino S, et al. Shape-driven response of gold nanoparticles to X-rays. Nanomaterials. 2023;13(19):2719. https://doi.org/10.3390/nano13192719.
39. De Matteis V, Cascione M, Rizzello L, Manno DE, Di Guglielmo C, Rinaldi R. Synergistic effect induced by gold nanoparticles with polyphenols shell during thermal therapy: macrophage inflammatory response and cancer cell death assessment. Cancers. 2021;13(14):3610. https://doi.org/10.3390/cancers13143610.
40. Mehrnia SS, Hashemi B, Mowla SJ, Arbabi A. Enhancing the effect of 4 MeV electron beam using gold nanoparticles in breast cancer cells. Physica Med. 2017;35:18–24. https://doi.org/10.1016/j.ejmp.2017.02.014.
41. Franken NAP, Rodermond HM, Stap J, Haveman J, Van Bree C. Clonogenic assay of cells in vitro. Nat Protoc. 2006;1(5):2315–9. https://doi.org/10.1038/nprot.2006.339.
42. M. Bajpayee, A. Kumar, and A. Dhawan, 'The Comet Assay: Assessment of In Vitro and In Vivo DNA Damage', in *Genotoxicity Assessment*, vol. 1044, A. Dhawan and M. Bajpayee, Eds., in Methods in Molecular Biology, vol. 1044. , Totowa: Humana Press, 2013, pp. 325–345. https://doi.org/10.1007/978-1-62703-529-3_17.
43. Prakash K, et al. History, introduction, and physiochemical properties of gold nanoparticles. Gold Nanopart Drug Deliv. 2024. https://doi.org/10.1016/B978-0-443-19061-2.00014-6.
44. Retif P, et al. Nanoparticles for radiation therapy enhancement: the key parameters. Theranostics. 2015;5(9):1030–44. https://doi.org/10.7150/thno.11642.
45. De Matteis V, Rizzello L, Di Bello MP, Rinaldi R. One-step synthesis, toxicity assessment and degradation in tumoral pH environment of SiO_2@Ag core/shell nanoparticles. J Nanopart Res. 2017;19(6):196. https://doi.org/10.1007/s11051-017-3870-2.
46. Gurunathan S, Han J, Park JH, Kim J-H. A green chemistry approach for synthesizing biocompatible gold nanoparticles. Nanoscale Res Lett. 2014;9(1):248. https://doi.org/10.1186/1556-276X-9-248.
47. Bhattacharya T, et al. Novel green approaches for the preparation of gold nanoparticles and their promising potential in oncology. Processes. 2022;10(2):426. https://doi.org/10.3390/pr10020426.
48. Thipe VC, et al. Green nanotechnology—an innovative pathway towards biocompatible and medically relevant gold nanoparticles. J Drug Deliv Sci Technol. 2022;70: 103256. https://doi.org/10.1016/j.jddst.2022.103256.
49. Lee KX, et al. Recent developments in the facile bio-synthesis of gold nanoparticles (AuNPs) and their biomedical applications. IJN. 2020;15:275–300. https://doi.org/10.2147/IJN.S233789.
50. A. O. Falade, K. E. Adewole, A.-R. O. Adekola, H. A. Ikokoh, K. Okaiyeto, and O. O. Oguntibeju, 'Aqueous extract of bay leaf (Laurus nobilis) ameliorates testicular toxicity induced by aluminum chloride in rats', *Vet World*, 2022, https://doi.org/10.14202/vetworld.2022.2525-2534.

51. Dias MI, et al. Nutritional and antioxidant contributions of *Laurus nobilis* L. leaves: would be more suitable a wild or a cultivated sample? Food Chem. 2014;156:339–46. https://doi.org/10.1016/j.foodchem.2014.01.122.
52. Ailli A, et al. Phytochemistry and biological activities of essential oils from six aromatic medicinal plants with cosmetic properties. Antibiotics. 2023;12(4):721. https://doi.org/10.3390/antibiotics12040721.
53. Tripathi RM, Yoon S-Y, Ahn D, Chung SJ. Facile synthesis of triangular and hexagonal anionic gold nanoparticles and evaluation of their cytotoxicity. Nanomaterials. 2019;9(12):1774. https://doi.org/10.3390/nano9121774.
54. Xie X, Liao J, Shao X, Li Q, Lin Y. 'The effect of shape on cellular uptake of gold nanoparticles in the forms of stars rods, and triangles.' Sci Rep. 2017;7(1):3827. https://doi.org/10.1038/s41598-017-04229-z.
55. Bandyopadhyay S, et al. Growing gold nanostructures for shape-selective cellular uptake. Nanoscale Res Lett. 2018;13(1):254. https://doi.org/10.1186/s11671-018-2662-7.
56. Polat O, Karagoz A, Isık S, Ozturk R. Influence of gold nanoparticle architecture on in vitro bioimaging and cellular uptake. J Nanopart Res. 2014;16(12):2725. https://doi.org/10.1007/s11051-014-2725-3.
57. Saqr A, et al. Synthesis of gold nanoparticles by using green machinery: characterization and in vitro toxicity. Nanomaterials. 2021;11(3):808. https://doi.org/10.3390/nano11030808.
58. Prades-Sagarra È, Yaromina A, Dubois LJ. Polyphenols as potential protectors against radiation-induced adverse effects in patients with thoracic cancer. Cancers. 2023;15(9):2412. https://doi.org/10.3390/cancers15092412.
59. Faramarzi S, Piccolella S, Manti L, Pacifico S. Could polyphenols really be a good radioprotective strategy? Molecules. 2021;26(16):4969. https://doi.org/10.3390/molecules26164969.
60. Nagpal I, Abraham SK. Protective effects of tea polyphenols and β-carotene against γ-radiation induced mutation and oxidative stress in Drosophila melanogaster. Genes Environ. 2017;39(1):24. https://doi.org/10.1186/s41021-017-0084-x.
61. Wang EJ-Y, et al. Alterations of cytoskeleton networks in cell fate determination and cancer development. Biomolecules. 2022;12(12):1862. https://doi.org/10.3390/biom12121862.
62. Schöchlin M, Weissinger SE, Brandes AR, Herrmann M, Möller P, Lennerz JK. A nuclear circularity-based classifier for diagnostic distinction of desmoplastic from spindle cell melanoma in digitized histological images. J Pathol Inform. 2014;5(1):40. https://doi.org/10.4103/2153-3539.143335.
63. Chhabra ES, Higgs HN. The many faces of actin: matching assembly factors with cellular structures. Nat Cell Biol. 2007;9(10):1110–21. https://doi.org/10.1038/ncb1007-1110.
64. Kalies S, et al. Investigation of biophysical mechanisms in gold nanoparticle mediated laser manipulation of cells using a multimodal holographic and fluorescence imaging setup. PLoS ONE. 2015;10(4): e0124052. https://doi.org/10.1371/journal.pone.0124052.
65. Schliwa M, Van Blerkom J, Pryzwansky KB. Structural organization of the cytoplasm. Cold Spring Harb Symp Quant Biol. 1982;46:51–67. https://doi.org/10.1101/SQB.1982.046.01.009.
66. Arjona MI, Najafi J, Minc N. Cytoplasm mechanics and cellular organization. Curr Opin Cell Biol. 2023;85: 102278. https://doi.org/10.1016/j.ceb.2023.102278.
67. Byrne HL, McNamara AL, Domanova W, Guatelli S, Kuncic Z. Radiation damage on sub-cellular scales: beyond DNA. Phys Med Biol. 2013;58(5):1251–67. https://doi.org/10.1088/0031-9155/58/5/1251.
68. Strobl JS, Melkoumian Z, Peterson VA, Hylton H. The cell death response to γ-radiation in MCF-7 cells is enhanced by a neuroleptic drug, pimozide. Breast Cancer Res Treat. 1998;51(1):83–95. https://doi.org/10.1023/A:1006046604062.